A High-Resolution Temperature-Salinity Dataset Observed by Autonomous Underwater Vehicles for the Evolution of Mesoscale Eddies and Associated Submesoscale Processes in South China Sea

Chunhua Qiu[1,2], Zhenyang Du[1,2], Haibo Tang[1,2], Zhenhui Yi[1,2], Jiawei Qiao[1,2], Dongxiao Wang[1,2,*] , Xiaoming Zhai[3], Wenbo Wang[1,2]

1. School of Marine Sciences, State Key Laboratory of Environmental Adaptability for Industrial Products, Sun Yat-Sen University, and Southern Marine Science and Engineering Guangdong Laboratory (Zhuhai), Zhuhai, China

2. Guangdong Provincial Key Laboratory of Marine Resources and Coastal Engineering, School of Marine Sciences, Sun Yat-sen University, Guangzhou 510275, China

3. Centre for Ocean and Atmospheric Sciences, School of Environmental Sciences, University of East Anglia, Norwich, UK

Corresponding author:

Dongxiao Wang

School of Marine Sciences,

Sun Yat-sen University

Email: dxwang@mail.sysu.edu.cn

Abstract. Marginal seas are often characterized by dynamic mesoscale eddies (MEs), whose evolution plays a critical role in regulating global oceanic energy budgets, triggering submesoscale processes with strong vertical velocity, and facilitating biogeochemical transport. However, traditional observation methods, constrained by passive sampling modes, struggle to resolve the temporal evolution of MEs and associated submesoscale processes at kilometer-scale resolutions. Autonomous underwater vehicles (AUVs) and underwater gliders (UGs), operating in active sampling modes, provide spatio-temporal synchronized measurements of these highly dynamic features. Here, we present a 9-year (2014-2022) high-resolution temperature-salinity dataset collected by AUVs/UGs in the South China Sea (SCS), accessible via https://doi.org/10.57760/sciencedb.11996 (Qiu et al., 2024b). In total, the dataset comprises 11 cruise experiments, deploying 50 UGs and 2 AUVs, achieving spatial and temporal resolutions of <7 km and <7 hours. This dataset offers unprecedented insights into ME evolution life stages, covering the zones of eddy's birth, propagation, and dissipation. 40% of the data resolve submesoscale processes (<1 km, <4 hours), capturing dynamic instabilities along and across frontal zones at eddy peripheries. This dataset has potential in improving the forecast accuracy in physical and biogeochemistry numerical model. Much more aggressive field investigation programs will be promoted by the NSFC in future.

Keywords: Autonomous Underwater Vehicles; Mesoscale eddies; Submesoscale processes; South China Sea

1. Introduction

Evolution of mesoscale eddies (MEs), characterized by intense geostrophic strain rates, leads to the generation of submesoscale processes with kilometer-scale spatial resolutions (McWilliams, 2016). This dynamic interplay requires observational systems with high spatio-temporal synchronization and enhanced resolution capabilities. MEs obtain kinetic energy from large-scale currents, and subsequently dissipate to submeso- or finer-scale processes in the slope regions via combined shear and baroclinic instabilities (Oey, 1995; Okkonen et al., 2003). Marginal seas (such as, Gulf of Mexico, Mediterranean) are usually filled with MEs (Rossby number $R_o = U/fL \approx 0.1$), alongside smaller-scale processes ($R_o > 1$). The South China Sea (SCS), as a tropical marginal sea, demonstrates particularly vigorous ME dynamics (Chen et al., 2011; Wang et al., 2003; Xiu et al., 2010). These coherent vortices, spanning 50–300 km horizontally and persisting several weeks to months, play vital roles in the transport of matter and energy (Chelton et al., 2007; Morrow et al., 2004).

Contemporary observation platforms for MEs include shipborne surveys, satellite remote sensing, Argo float arrays, Lagrangian drifters, autonomous underwater vehicles (AUVs), and underwater gliders (UGs). While ship-based observations are the most fundamental to investigate the MEs' general structures, their temporal resolution limits continuous evolution tracking. Satellite altimetry provides comprehensive surface signatures of MEs, including spatial-temporal metrics, radius evolution, and trajectory mapping (Chelton et al., 2011). Four primary ME generation hotspots have been identified in the SCS: southwest of Taiwan, northwest of Luzon Islands, the Xisha Islands region, and the eastern Vietnamese coastal zone (Hwang et al., 2000; Wang et al., 2003; Nan et al., 2011). ME propagation patterns (westward, southwestward, or northwestward) are predominantly governed by first-baroclinic Rossby wave dynamics (Lin et al., 2007; Xiu et al., 2010; Chen et al., 2011). Since 2002, a large number of Argos have been deployed, providing routine measurements to describe vertical structures of MEs (He et al., 2018; Table 1). However, the spatio-temporal resolutions of Argo profiles are approximately 100 km and 10 days, remaining insufficient to capture the high-frequency variability of MEs and submesoscale processes (Table 1).

Table 1. Previous observational studies of mesoscale eddies (MEs) in South China Sea.

Platforms	Authors	ME Sources
Ship Observation (CTD Station)	Dale, 1956	Cool pool near Vietnam
	Wang et al., 1987	Warm eddy near southwestern of Taiwan Islands
	Xu et al., 1997	Northwest of Luzon Islands, named Luzon cold eddy
	Li et al., 1998	A warm eddy in northeast of NSCS
	Chu et al., 1998	An eddy pair in central of SCS.
	Fang et al., 2002	Vietnam warm eddy
Satellite Observations (sea level anomaly; velocity)	Hwang et al., 2000; Wang et al., 2003; Nan et al., 2011	Topex/Poseidon altimeter data, 94 cold eddy, 124 warm eddy. Southwest of Taiwan Islands, northwest of Luzon Islands, East of Vietnam.
	Lin et al., 2007; Chen et al., 2011; Xiu et al., 2010	Radius, life cycle, tracking, seasonal and interannual variations of mesoscale eddies
	He et al., 2016	The role of ENSO on interannual variation in Luzon Strait mesoscale eddies
	He et al., 2019	MEs' influence on Chlorophyll-a
Argo; Mooring	Li et al., 2022	Vertical tilt of Mesoscale eddy
	He et al., 2018	Reconstruction data combine altimeter and Argos, revisit the three-dimensional structures of ME
	Zhang et al., 2017	By using mooring array, investigate eddy looping from Luzon Strait

Attributed to the active tracking, AUVs and UGs become more and more important tools in exploring marine environment over last two decades. They have the advantages in low cost, long-duration, controllability and reusability. Our research consortium has acquired high-resolution spatio-temporal datasets through coordinated UG and AUV deployments across ME features. UGs became available to the marine science community in 2004, and they adjust buoyancy to generate gliding motion through water columns by a pair of wings (Rudnick et al., 2004; Caffaz et al., 2010). These UG platforms execute "sawtooth" transects at sustained velocities of ~0.3 m/s, while AUVs are propeller-driven, acting as combining "sawtooth" and "cruise" modes at the maximum speed of 1 m/s (Hobson et al., 2012). For a representative SCS ME with 100 km radius, full feature transection requires approximately 2.7 days for either platform type. Both platforms carry conductivity-temperature-depth (CTD) sensors for concurrent thermohaline structure mapping, enabling successful detection of dynamic features, such as the warming trend in Gulf Stream (Todd and Ren, 2023), and the water mass exchanges between Bay of Bengal and Arabian Sea (Rainville et al., 2022). Our systematic observation program initiated UG deployments in 2014 (Qiu et al., 2015), and commenced AUV field campaigns in 2018 (Huang et al., 2019; Qiu et al., 2020). We present a consolidated 9-year dataset (2014-2022) from SCS operations, demonstrating unique capabilities of these platforms in resolving ME evolution dynamics and associated submesoscale processes.

2 Datasets

2.1 UG and AUV Experiment Sites

Our experimental design specifically targeted ME evolution and submesoscale process characterization. This study employs two types of Chinese-developed UG platforms: the "Sea-Wing" (Yu et al., 2011) and "Petrel" (Wu et al., 2011). Since 2014, we have conducted 11 field campaigns in the northern SCS, deploying 50 UGs and 2 AUVs to collect 13,491 temperature-salinity profiles. Platform deployment parameters, including the deploying time, installed sensors, and diving depths of UGs/AUVs experiment are shown in Table 2. Complete mission metadata (vehicle serial number, waypoints, matching time, latitude, and longitude) are archived in the data with *.nc format. The gray shading in Table 2 highlights the UG arrays consisting of ≥3 units. Notably, in the experiments of 2017, 2019 and 2020, more than 10 UGs were deployed to resolve the three-dimensional structures of the MEs.

Table 2. Available data sets from UG or AUV

ME: Mesoscale Eddy; AUV: Autonomous Underwater Vehicle; UG: Underwater Glider.

Number	Equipment	Time	Number of Qualified Profiles	Number of Eliminated Profiles (Stage)	Number of equipment	Sensor of equipment (*: with Shipped CTD)	Diving depth of equipment	Observing Purpose
1	UG	Sept. 19- Oct. 15, 2014; 26 days	227	0	1 UG	Seabird Glider Payload CTD(GPCTD)	1000 m	Mixed layer heat budget; sea trials
2	UG	Apr. 18-Jul. 6, 2015; 78 days	1358	1(Syntax_Test)	3 UGs Network	Seabird Glider Payload CTD(GPCTD)	1000 m	Structures of ME
3	UG	Jul. 14-UG. 13, 2017 30 days	2902	99(Syntax Test)	10 UGs, Network	Seabird Glider Payload CTD(GPCTD)	300 m (3) 1000 m (7)	ME response to TC
4	UG	Apr. 22-May 23, 2018; 31 days	239	0	1 UG, Virtual mooring	Seabird Glider Payload CTD(GPCTD)	1000 m	Structures of ME
5	UG	Jul. 13- Sept. 30, 2019; 77 days	3672	0	17 UGs, Network	Seabird Glider Payload CTD(GPCTD) *	1000 m (17)	Slope intrusion of ME
6	AUV	Sept. 18- Oct. 23, 2019; 35 days	131	0	1 AUV	SBE37 CTD; DVL^{++}	300 m	Evolution of ME
7	UG	Jun. 26- Aug. 27, 2020; 60 days	3793	7(Syntax Test)	12 UGs	Seabird Glider Payload CTD(GPCTD)	1000 m	Slope current
8	UG	Jul. 26- Aug. 8, 2021; 13 days	307	155(Climatology_Test & Syntax_Test);	2 UGs	RBR legato CTD	300 m (1) 1000 m (1)	Edge of ME
9	UG	Aug. 7- Aug. 27, 2021; 20 days	215	0	2 UGs	Seabird Glider Payload CTD(GPCTD)	1000 m	Edge of ME
10	AUV	May 9- Jul. 29, 2021; 80 days	168	0	1 AUV	SBE37 CTD	300 m	Evolution of ME
11	UG	Jun. 23- Jul. 6, 2022; 13 days	217	0	2 UGs	Seabird Glider Payload CTD(GPCTD)	1000 m	Edge of ME
Total	/	463 days	13229	262	50 UGs, 2 AUVs	/	/	Structures and evolution of ME

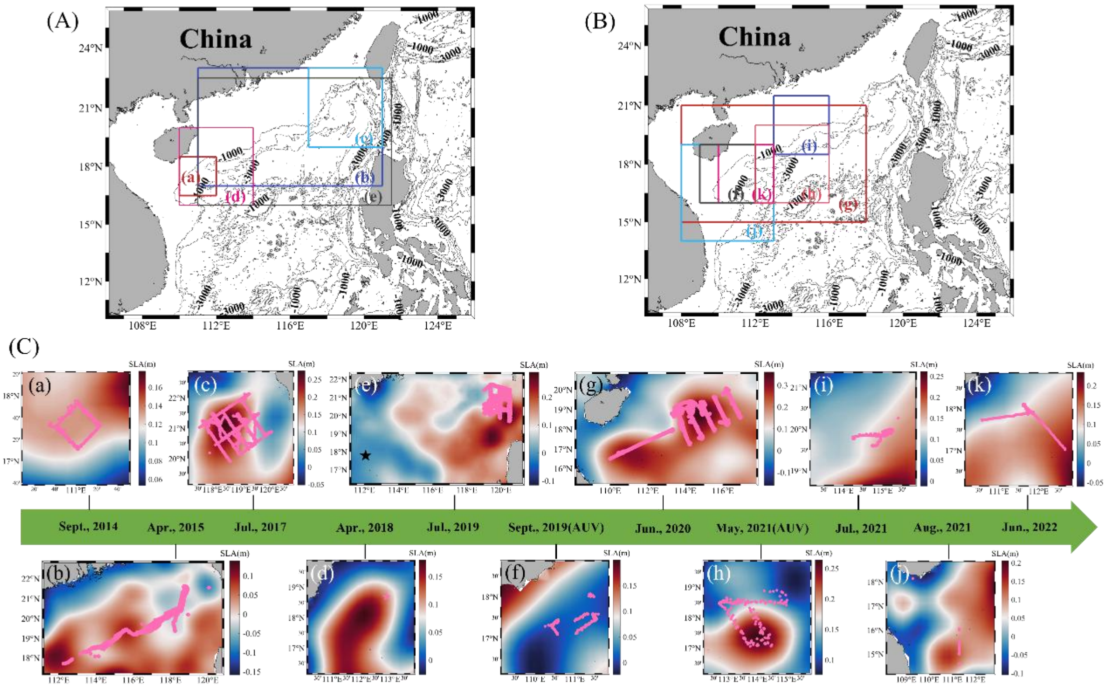

Figure 1. Underwater glider (UG) and autonomous underwater vehicle (AUV) observation sites. (A) observation area for subplots (a)-(e); (B) area for subplots (f)-(j). The grey lines in (A) and (B) are the water depth. (a)-(j) Observation stations (pink dots) with mean sea level anomaly (shading colors). The observation times are (a) September 2014; (b) April 2015; (c) July 2017; (d) April 2018; (e) July 2019; (f) September 2019; (g) June 2020; (h) May 2021; (i) July 2021; (j) August 2021; and (k) June 2022.

2.2 Intercomparison of UGs and AUVs Resolution

The trajectories of AUVs and UGs are depicted in Figure 1. Each trajectory is superimposed on sea level anomaly (SLA) fields. The maximum absolute value of SLA is the ME center. Note that all the UGs and AUVs crossed MEs. Spatio-temporal sampling characteristics are presented in Figure 2. The horizontal resolution reveals two distinct regimes: 4-7 km resolution dominated 2014, 2015, and 2019 campaigns (blue histograms), while sub-3 km sampling was achieved in other years. Temporal sampling intervals exhibited similar bimodal distribution, reaching optimal 1-2 hours cadence during the 2017, July 2021, and 2022 deployments (Figures 2c, 2f, 2h), compared to 4-7 hours resolutions in remaining experiments. This observational matrix demonstrates that 100% of datasets resolve ME-scale dynamics (50-300 km spectral range), while 40% of campaigns attained sufficient resolution to capture submesoscale features (<3 km; <4 hours characteristic scale) through synergistic AUG/AUV coordination.

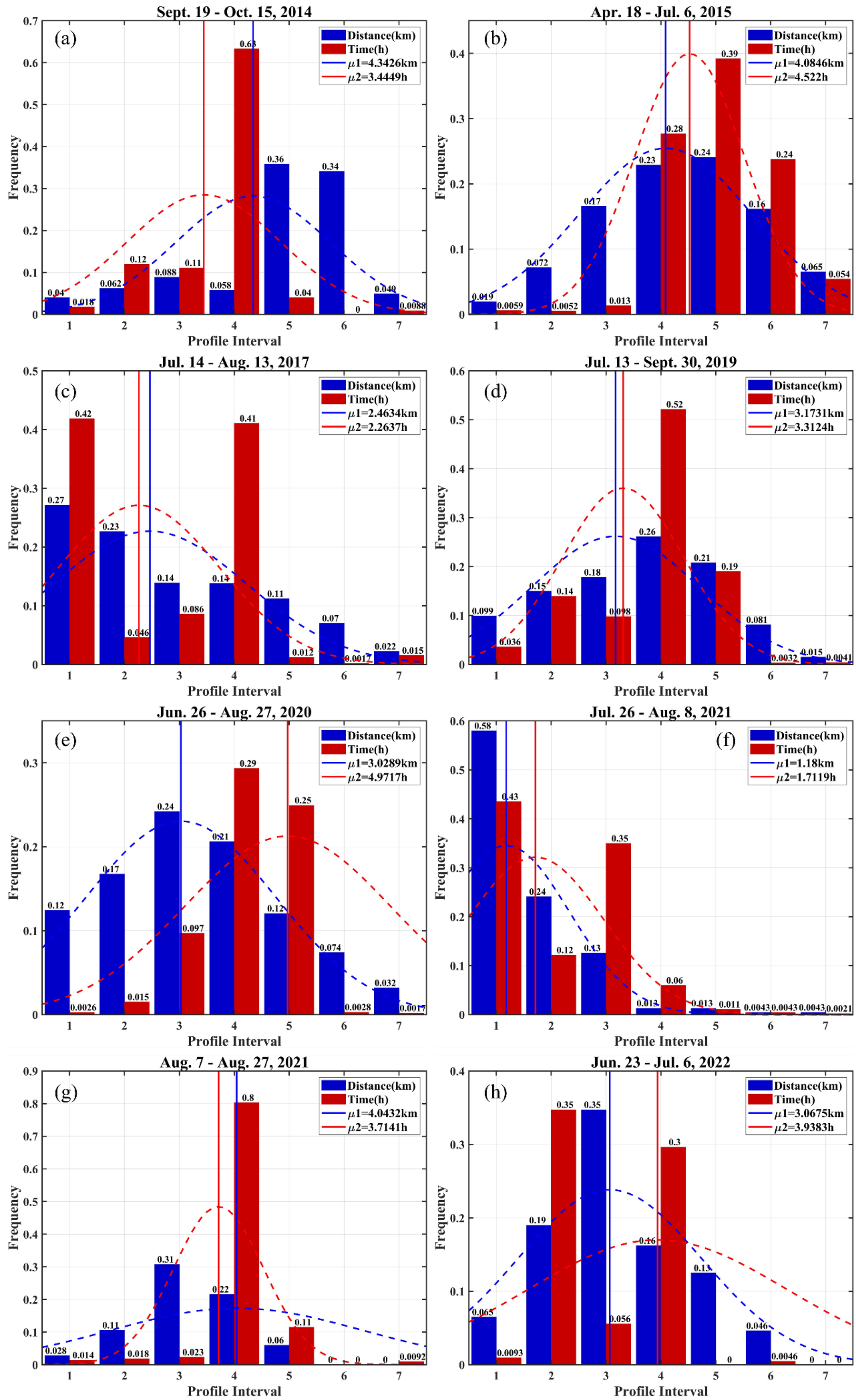

Figure 2. Frequency of spatial (blue bar) and temporal (red bar) sample interval. “Profile interval” indicates the spatial interval (red) and temporal interval (blue). Bars are the probabilities. Dashed lines are normal distributions of spatial interval (red) and temporal intervals (blue). Mean values

of spatial and temporal intervals are depicted in red and blue solid lines.

3 Data Quality Control Method

Prior to investigating the three-dimensional structures of MEs, we did rigorous data quality-control (QC) for the UGs and AUVs datasets.

3.1 UG data Quality Control

Two products of Chinese UGs named "Sea-wing" and "Petrel" were employed in this study. These platforms integrate communication and navigation subsystems comprising: iridium satellite communication devices, wireless communication devices, a precision navigation attitude sensor, a Global Positioning System (GPS) device, a pressure sensor, an obstacle avoidance sonar and CTD sensor with 6-second sampling interval.

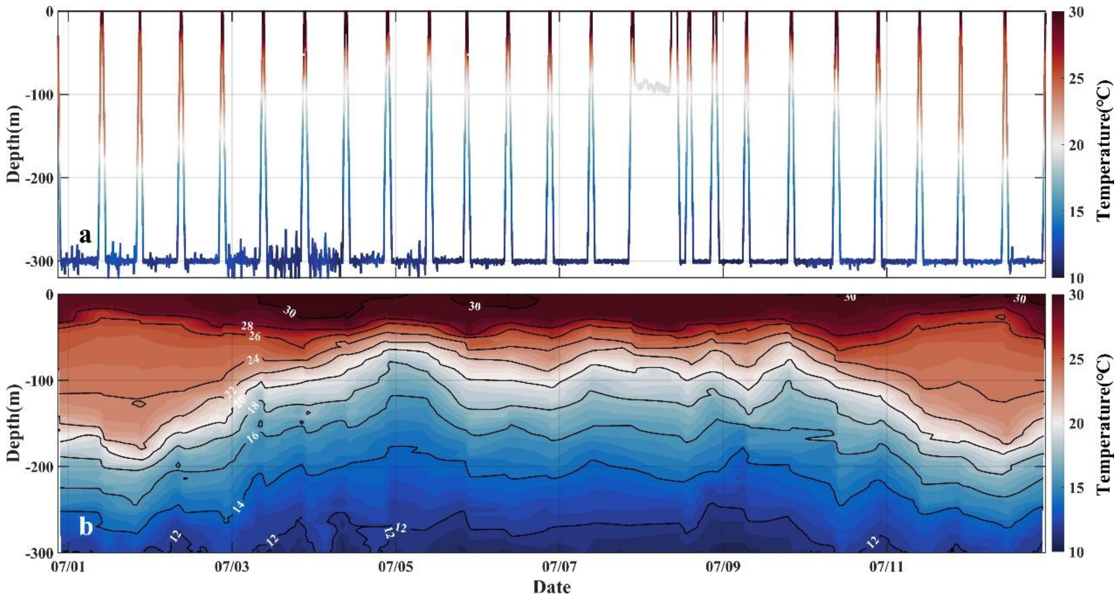

Figure 3. Illustration of (a) original, and (b) interpolated data after quality control. The AUV duration is in July 2021. AUV: autonomous underwater vehicle.

Before investigating oceanic phenomena, we did data quality control following the standard of integrated ocean observing system (IOOS). The QC procedure for UG (https://repository.oceanbestpractices.org/handle/11329/289?show=full) includes 9 steps: (1) Timing/Gap Test: Test determines that the profile has been received within the expected time window and has the correct time stamp; (2) Syntax Test: Ensures the structural integrity of data messages; (3) Location Test: Test if the reported physical location (latitude and longitude) is within the reasonable range determined by the operator; (4) Gross Range Test: Ensure that the data points do not exceed the minimum/maximum output range of the sensor; (5) Pressure Test: Test if the pressure records increase monotonically with depth, sorted the vertical depth values and removed any duplicate depth values; Data after steps (1)-(5) are directly output from UGs. (6) Climatology Test: Test if the data points are within the seasonal expectation range; (7) Spike Test: Test if the data points exceed the selected threshold compared to adjacent data points, excluded the data with temperature/salinity larger than 35 ℃/35 psu. (8) Rate of Change Test: Test if the rate of change in the time series exceeds the threshold determined by the operator; (9) Flat Line Test: Test for continuously repeated observations of the same value, which may be the result of sensor or data collection platform failure. Post-Stage (6) & (7) data are designated as *_RO (Remove Outliers), while Stages (8)-(9) outputs generate *_TSD (Triple Standard Deviation) following 3σ outlier exclusion.

We performed cross-validation using the UG observed temperature and salinity profiles and shipborne CTD casts data during July 2019 (black star in Figure 1e; Figure 4). Quantitative analysis revealed the mean bias of temperature is 0.05 ℃, and that of salinity is 0.01 psu. The vertical temperature/salinity profiles observed by ship and UG are consistent, supporting that the data are credible.

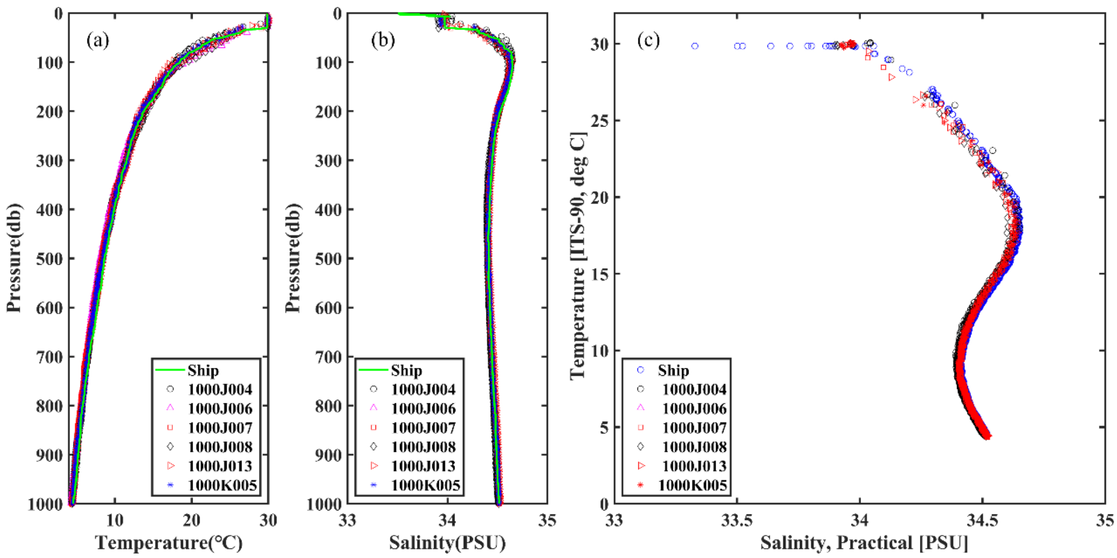

Figure 4. Comparison of (a) temperature, (b)salinity, and (c) temperature-salinity scatter plots between ship installed CTD and AUV installed CTD at station (112.0661°E, 17.7778°N). Green line in (a) and (b) is the ship measured values. Dot, pink triangle, red square, diamond, red

triangle, and blue star are for UGs named 1000J004, 1000J006, 1000J007, 1000J008, 1000J013 and 1000K005, respectively.

3.2 AUV Data Quality Control

Both CTD and GPS instrument were installed on the "Sea-Whale 2000" AUV. The platform was designed by Institute of Shenyang Automation, Chinese Academy of Sciences. It could operate in two modes: "sawtooth" mode and "cruise" mode at a specific depth of 300 m (Huang et al., 2019).

For "sawtooth" mode data, we applied identical quality control protocols as described in Section 3.1 for UGs (Figures 3-4). In "cruise" mode, the AUV navigates at the depth of around 300 m. Following Qiu et al (2020), we, first, transformed the temperature and salinity at depth z to those at 300 m using a linear regression method ($T' = 0.008z' + 0.017; S' = -0.0002z' + 0.0006$),

$$T' = T_z - T_{mean}, \tag{1a}$$

$$S' = S_z - S_{mean}, \tag{1b}$$

where T_{mean} is averaged using a 10-point smooth average, which could maintain the spatial variations from 20 to 30 km. Depth anomaly is defined as the measured depth minus 300 m, $z' = z - 300$, and the temperature and salinity anomalies as $T'$and S', respectively. Validation against potential temperature algorithm demonstrated the temperatures reconstructed at 300 m were highly consistent.

3.3 Density Derived from Temperature and Salinity

Seawater density (ρ, in kg/m^3) was computed based on temperature (T in °C), salinity (S in psu), and pressure (P in dbar) using the UNESCO international equation of state (Fofonoff and Millard, 1983). The UNESCO formula provides a simplified approach to estimate seawater density as follows:

$$\rho(S,T,P) = \frac{\rho_0(S,T)}{1 - \frac{P}{K(S,T,P)}} \tag{2a}$$

$$\rho_0(S,T) = \rho_{sw}(T) + (b_0 + b_1T_{68} + b_2T_{68}^2 + b_3T_{68}^3 + b_4T_{68}^4)S \\ +(c_0 + c_1T_{68} + c_2T_{68}^2)S\sqrt{S} + d_0S^2 \tag{2b}$$

$$\rho_{sw}(T) = a_0 + a_1 T_{68} + a_2 T_{68}^2 + a_3 T_{68}^3 + a_4 T_{68}^4 + a_5 T_{68}^5 \tag{2c}$$

$$T_{68} = T \times 1.00024 \tag{2d}$$

where $K(S, T, P)$ is secant bulk modulus, a_0 and others are coefficients. Coefficients follow the original formulation accounting for nonlinear compressibility effects.

4. Data Application

4.1Subsurface MEs Observed by UGs and AUVs

Glider arrays successfully captured full-depth thermohaline signatures of both warm and cold eddies through cross-eddy transects (Figure 4). In April 2015, one UG deployment crossed a warm eddy, and observed a subsurface warm core (Figures 1b & 5a), corresponding to the subsurface eddy (50-500 m depth, 100 km radius) as described by Shu et al. (2016). Qiu et al (2019) utilized this dataset to investigate the asymmetry structures of this subsurface eddy, suggesting that the centrifugal force should be taken into account when revealing the velocity of MEs, i.e., gradient wind balance theory. June 2020 glider observations captured a subsurface cold eddy exhibiting pronounced thermohaline anomalies within the main pycnocline layer (Figures 1g & 5d-f). This density-compensated structure, defined as local deviations from zonal mean conditions, manifested through compensating temperature and salinity anomalies that generated a baroclinic density core penetrating the upper 500 m. The colocated thermohaline signatures demonstrate UG's capability in resolving three-dimensional eddy characterization, including core localization, spatial footprint delineation, and dynamic intensity assessment.

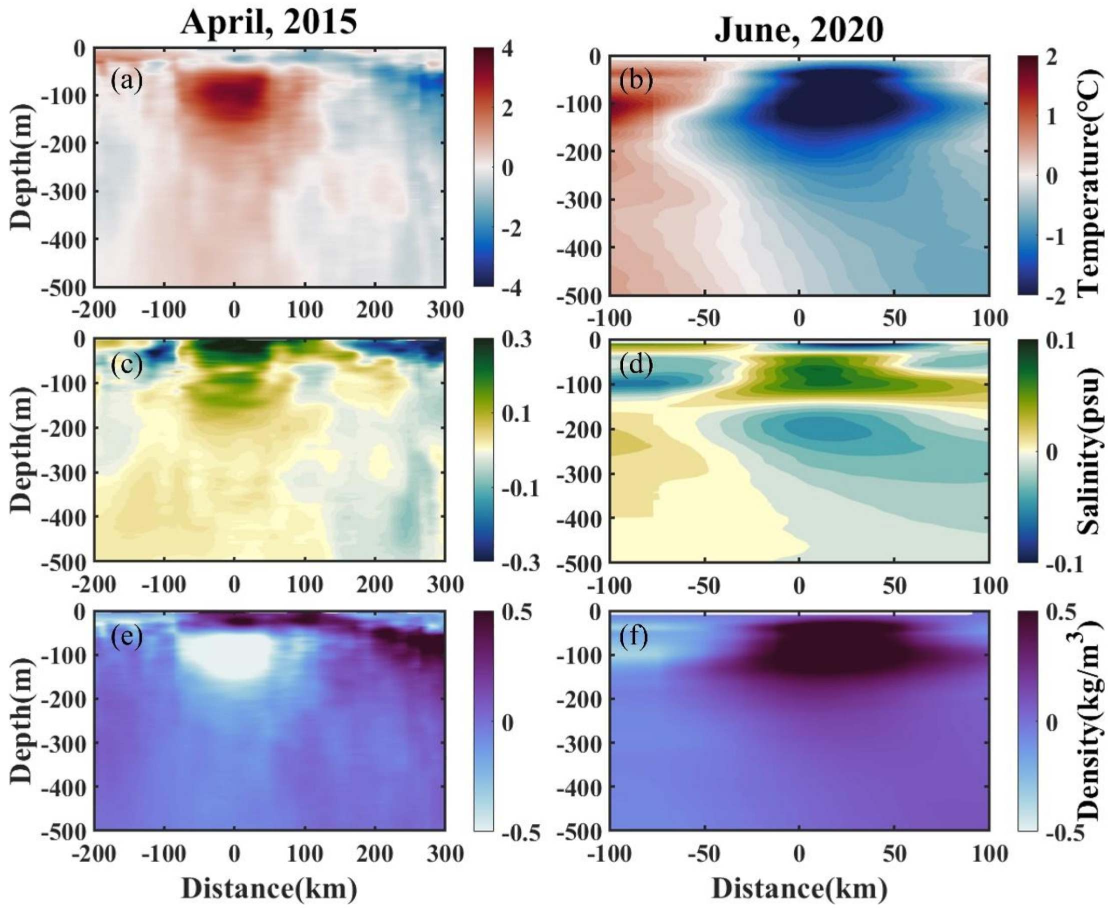

Figure 5. Contour of (a) and (b) temperature anomaly (c) and (d) salinity anomaly, (e) and (f) density anomaly in April, 2015(left panels) and June, 2020(right panels). The contours were generated using interpolation of the original data points.

Both UG and AUV demonstrate capability in monitoring the temporal evolutions of subsurface MEs. During their developmental stages, these vortices exhibit morphological instabilities that induce cross-slope transport along continental margins (Wang et al., 2018; Su et al., 2020; Qiu et al., 2022), while simultaneously generating submesoscale processes through frontal instability (Dong et al., 2018; Yang et al., 2019). To capture eddy evolution process, we executed five successive AUV transects along rectangular trajectories across an anticyclonic ME during May to July 2021 (Figure 1h), supported by the National Key Research and Development Program.

Figure 6 illustrates a subsurface-intensified anticyclone occupying the 50-200 m depth stratum, exhibiting weakened stratification with reduced Brunt-Väisälä frequency squared value ($N^2 = \frac{1}{\rho}\frac{d\rho}{dz} < 10^{-4}$). The AUV mission was divided into five discrete phases: T1 (8-11 June), T2 (19-23 June), T3 (29 June-4 July), T4 (10-15 July), and T5 (21-26 July). Delineating the eddy boundaries using isopycnals at 22.5 kg m^{-3} and 23.5 kg m^{-3}, we quantified temporal variations in eddy area and thermal properties. A progressive decline in both areal extent and mean temperature occurred between T1 and T3, followed by subsequent recovery from T4 to T5, indicating distinct weakening and reintensification phases. This lifecycle aligns with Qiao et al.'s (2023) trajectory analysis documenting eastward propagation during T1-T3 and topographic trapping during T4-T5.

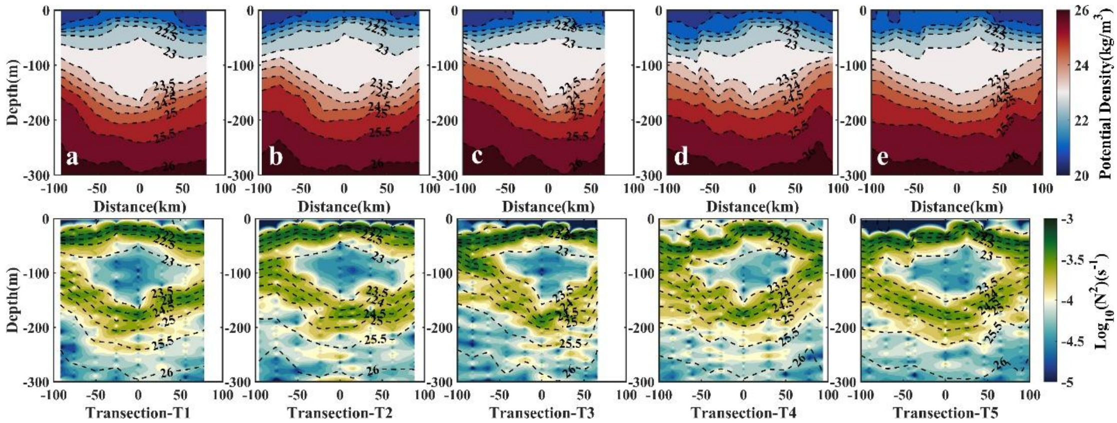

Figure 6. The profiles of density (upper panel) and Brunt frequency (lower panel) during (a,f)T1, (b,g)T2, (c,h)T3, (d, i)T4, (e, j)T5 period, which was 06/08-06/11,06/19-06/23,06/29-07/04,07/10-07/15,07/21-07/26, respectively. The contours were generated using interpolation of the original data points.

4.2 Vertical Tilt of MEs at Different Life-stages Observed by UGs

Coordinated glider deployments were executed in 2015, 2017, 2019, and 2020 to resolve ME dynamics. The complete ME lifecycle progresses through four distinct phases: birth, developing, mature and dissipation stages (Zhang and Qiu, 2018; Yang et al., 2019), with each phase exhibiting different kinetic energy budgets. The Luzon Strait serves as an eddy birth zone where Kuroshio branch intrudes the SCS (Chen et al., 2011; Su et al., 2020). After birth, most of the eddies move westward to the continental shelf zone under the modulation of Rossby wave, finally dissipate in Dongsha Islands, Xisha Islands or merged with other eddies (Yang et al., 2019; Su et al., 2020; Qiu et al., 2022).

These deployments of AUVs and UGs enabled three-dimensional structural characterization across ME life stages. Quality-controlled temperature-salinity profiles were interpolated into 1 km $\times$ 1 km $\times$ 1 m grids prior to density (ρ) computation. Assuming geostrophic balance, the geostrophic velocity, v_g, could be derived under the force balances between pressure gradient and Coriolis forces,

$$v_g(x,y,z) = v_0 - \frac{g}{f\rho_0}\int_{z0}^{z}\left(\frac{\partial\rho(x,y,z)}{\partial x} + \frac{\partial\rho(x,y,z)}{\partial y}\right)dz, \tag{3}$$

where ρ_0 is the referenced water density, f is the Coriolis frequency, and v_0 (set to 0) represents the referenced geostrophic velocity at depth 1000 m.

The July 2019 deployment (12 UGs, 120°E) observed the three-dimensional temperature and geostrophic velocity structures of a ME at birth stage, and captured the subsurface warm core exhibiting a northeastward vertical tilt (solid black line in Figure 7). July 2017 observations (10 UGs, 119°E) revealed a developing eddy that exhibited eastward tilt through 500 m water column, which may be attributed to combined forcing from westward-propagating Rossby waves and background current shear (e.g., Qiu et al., 2015; Zhang et al., 2016), as well as thermal front advection (e.g., Bonnici and Billant, 2020; Gaube et al., 2015). Throughout this experiment, the UGs encountered the tropical storm “Haitang”, resulting in that the ME underwent horizontal deformation and giving rise to submesoscale processes (Yi et al., 2022; Yi et al., 2024).

June 2020 observations (12 gliders; Figures 1g and 6e-h) documented a dissipating anticyclone with southwestward tilt from 500 m to surface (Figure 7e-7f). This kind of southwestward vertical tilt was revealed in a numerical model, which steep topography caused asymmetries of the velocities within the MEs (Qiu et al., 2022). June 2021 AUV measurements (Qiao et al., 2023; Figure1h) further captured an eastward movement of ME, which was dominated by wave-current interactions.

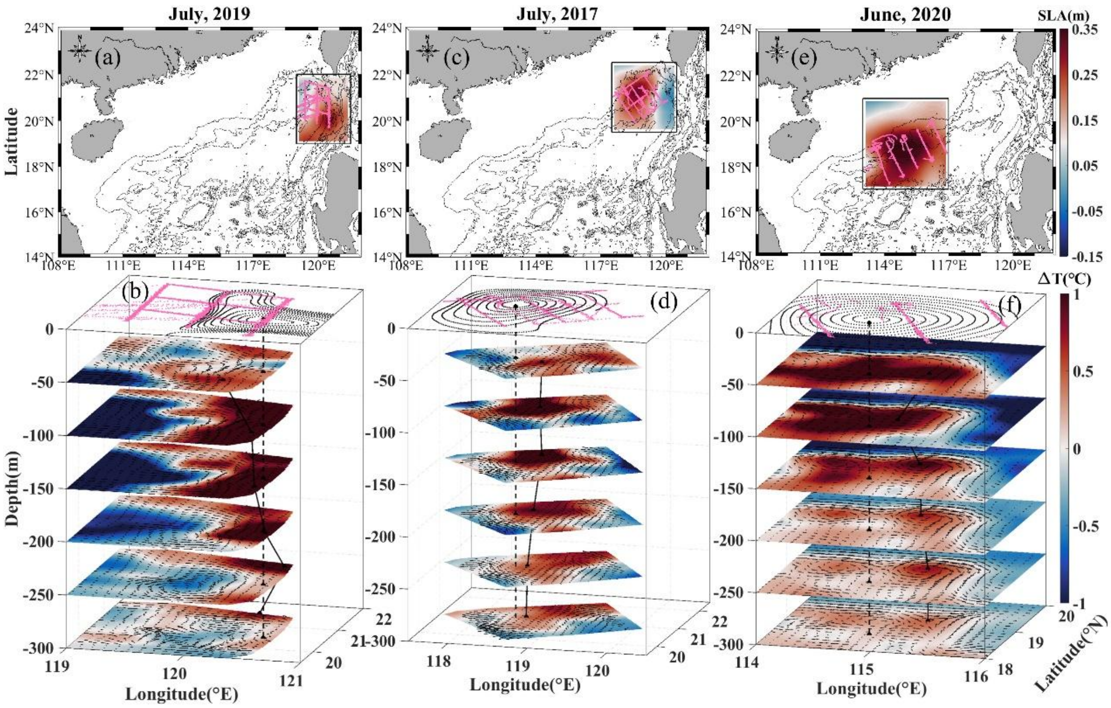

Figure 7. Eddy structures during periods of (a-b) eddy birth, (c-d) westward movement, and (e-f) dissipation along slope movements. Sea level anomaly (SLA) and UGs' positions are superimposed in upper panels (a, c, e), isobaths are represented by solid lines. The UG observed temperature and derived geostrophic velocities are in the 3D plots (b, d, f). Pink lines are the tracks of UGs. Dashed lines denote the centers of mesoscale eddies from SLA fields, and solid dot lines are the centers from warm cores. UG: Underwater Glider. The contours were generated using interpolation of the original data points.

4.3 Submesoscale Instabilities at the Edge of MEs Observed by UGs

Submesoscale process, usually occurs within MEs, either at the eddy peripheries (front; filament) or entrained in the eddy center, in terms of spiral structures or "eye-cat" structures (Zhang and Qiu, 2018; Ni et al., 2021; Hu et al., 2023; Qiu et al., 2024). These processes facilitate bidirectional energy transfers, driving forward cascades to dissipating scales through symmetric and centrifugal instabilities while simultaneously energizing inverse energy pathways to MEs via mixed-layer baroclinic instabilities (i.e., Fox-Kemper et al., 2008; McWilliams, 2016). Conventional Argo floats, constrained by 10-day sampling intervals, provide insufficient data to resolve rather short-time scale features. Recent technological advancement reveals diverse observational capabilities. For example, Lagrangian platforms, like NAVIS floats, have identified frontal genesis dominated by mixed-layer baroclinic instability (Tang et al., 2022), while glider arrays employing virtual mooring configurations achieve Eulerian frontal characterization through programmable sampling strategies (Qiu et al., 2019a; Shang et al., 2023). This methodological contrast highlights glider advantages in enabling simultaneous cross-front and along-front measurements through active navigation, overcoming the spatial limitations inherent to passive Lagrangian drifters.

Our observational dataset reveals that 40% of UG missions resolved submesoscale processes (<3 km horizontal resolution, <4 hours temporal resolution; Figure 2). To demonstrate this operational advantage, we have analyzed two representative cases of submesoscale instabilities along ME peripheries.

The 2017 deployment illustrates multi-platform sampling strategies, with four UGs strategically positioned at an anticyclonic ME boundary (Figure 8a). Three UGs executed cross-front transects while one maintained along-front tracking, enabling comprehensive instability characterization through the Richardson number phase angle, ϕ_{Ri}, as defined,

$$\phi_{Ri} = tan^{-1}\left(-\frac{1}{Ri}\right) = tan^{-1}\left(\frac{|\nabla \cdot b|^2}{N^2 \cdot f^2}\right), \tag{3a}$$

$$Ri \approx Ri_g = \frac{N^2}{\left(\frac{\partial \overline{v_g}}{\partial z}\right)^2} = \frac{N^2 \cdot f^2}{|\nabla \cdot b|^2} < \frac{f}{\zeta_g}, \text{ and } f \cdot \zeta_g > 0, \tag{3b}$$

where $b = -g\rho/\rho_0$, is the buoyancy flux, g is the gravitational acceleration. $N^2 = \partial b/\partial z$ is the vertical buoyancy frequency. $\zeta_g = curl(\overrightarrow{v_g})$ is the vertical relative vorticity (Thomas et al., 2013). For anticyclonic eddies, inertial instability or symmetric instability occurs when $-45° < \phi_{Ri} < \phi_c$. $\phi_c = \tan^{-1}\left(-(f + \zeta_g)/f\right)$ is the critical angle. Only symmetric instability occurs when $-90° < \phi_{Ri} < -45°$; symmetric instability or gravitational instability occurs when $-135° < \phi_{Ri} < -90°$; and gravitational instability occurs when $-180° < \phi_{Ri} < -135°$.

The 2017 dataset revealed coexisting gravitational, symmetric, and centrifugal-symmetric instabilities along the ME periphery (Figure 8a). Figure 8b shows submesoscale instabilities in 2019. In this case, gravity instability dominates the upper mixed layer, while symmetric and centrifugal instabilities are not significant. These two cases provide us enough information to detect frontal genesis processes in Eulerian view, while NAVIS or Argos provide frontal information in Lagrange view.

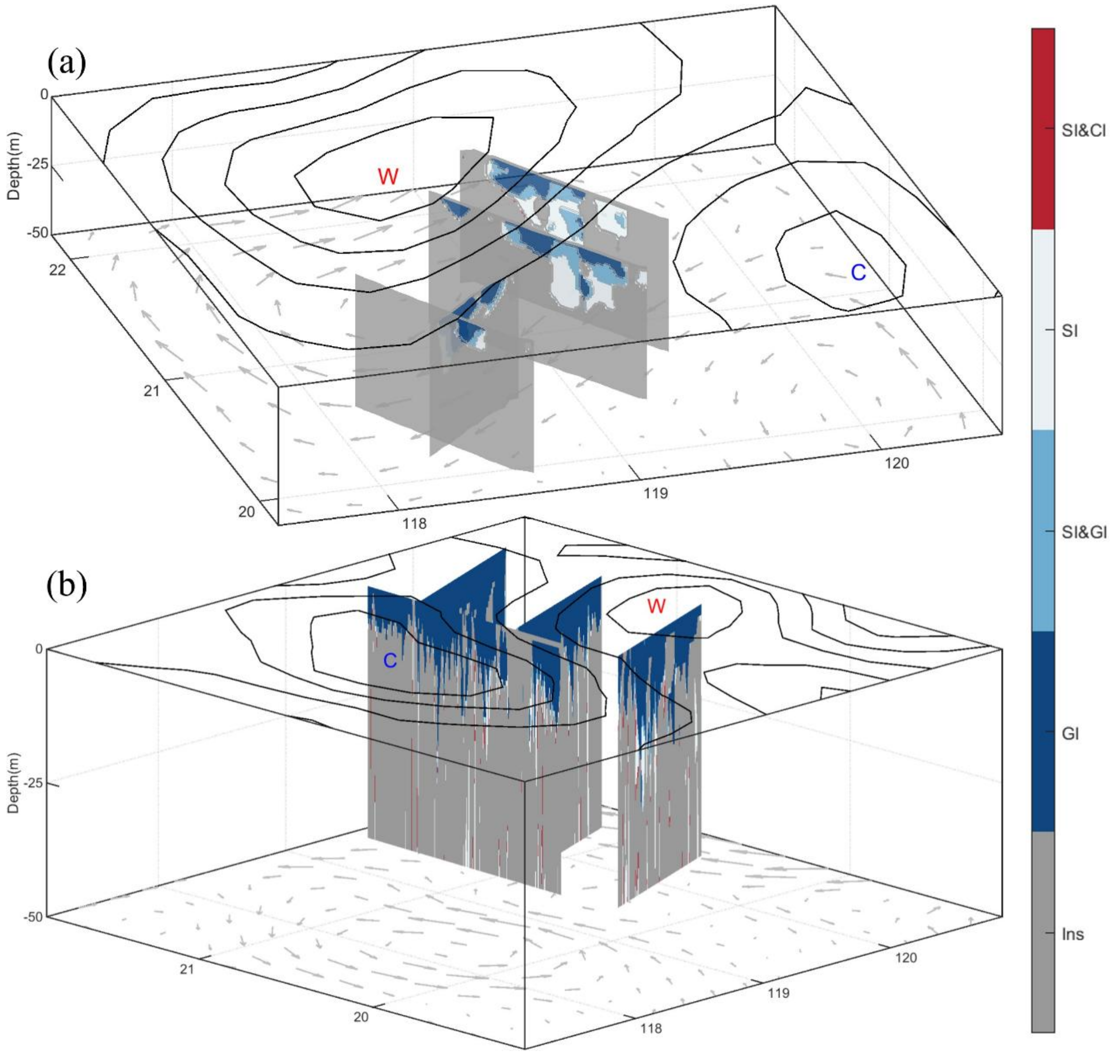

Figure 8. Analyzed submesoscale instabilities at the edge of mesoscale eddies. (a)in 2017, and (b) in 2019. SI: symmetric instability; CI: centrifugal instability; GI: gravity instability. W: anticyclonic eddy; C: cyclonic eddy. Isolines are the sea level anomaly. The contours were generated using interpolation of the original data points.

5. Data Availability

The dataset of temperature/salinity observed by AUV and UG in this manuscript was deposited in Science Data Bank, whose DOI is https://doi.org/10.57760/sciencedb.11996 (Qiu et al., 2024b). The dataset includes two files of "Grid_data" and "Observation_data".

6. Conclusions and Potential Future Plan

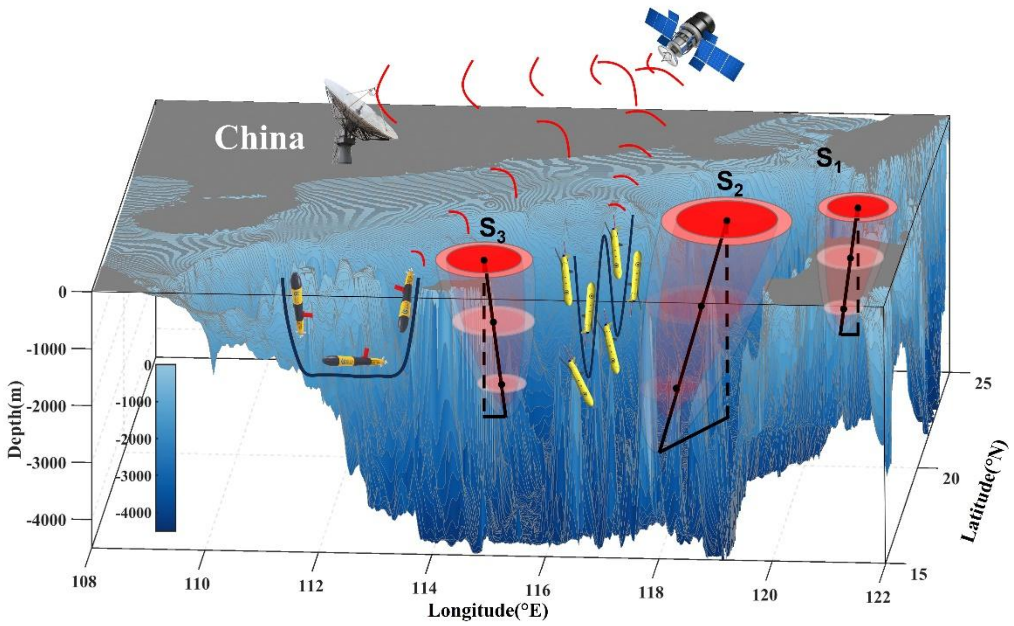

Figure 9. UG operations to observe mesoscale eddies at different life stages. S1: birth stage; S2: developing/mature stage; S3: dissipating stage. UG: Underwater Glider; SCS: South China Sea.

Our 9-year AUVs and UGs observations yielded a high-resolution temperature and salinity profiles dataset in SCS. This comprehensive compilation comprises 13,491 profiles and covers 463 days' experiments, encompassing 11 experiments deploying 50 UGs and 2 AUVs. To our knowledge, this represents the first multi-platform dataset with sufficient spatiotemporal coverage in detecting the horizontal asymmetry, vertical tilt, temporal evolution, life cycle of MEs (Figure 9), while simultaneously capturing associated submesoscale processes. The dataset allows us to investigate the subsurface MEs, revealing eddy-current and eddy-topography interactions successfully. However, quantifying ME feedbacks on the variability of larger scale current, i.e., western boundary current, long-term routine UGs and AUVs observations are needed in future.

Beyond tracking MEs, UGs and AUVs have been proved to actively capture smaller scale oceanic processes. Successful applications include internal tide (Gao et al., 2024) and turbulent dissipation rates by using turbulent parameterization schemes (Qi et al, 2020). Moreover, UGs/AUVs equipped with more sensors could also provide us geochemical parameters (e.g., Yi et al., 2022), potentially enhancing coupled physical-biogeochemical model ability forecasting through data assimilation. More projects gathering AUVs network are ongoing and will be promoted in future.

Operational challenges encountered during the program include: (1) under strong background current, UGs and AUVs get disturbed and cannot follow the customized routes; (2) during extreme meteorological conditions, it difficult for piloting team to deploy and recovery UGs and AUVs; (3) data receiving capacity depends on the satellite transmission capacity. If both the bio-chemistry and CTD data are included, the data resolution have to be lowered. Addressing these challenges requires synergistic collaboration between field operations teams, platform engineers, and dynamical oceanographers to optimize autonomous sampling systems.

Author Contributions

Conceptualization: DX; data curation: CH, ZY, ZH, JW; formal analysis: CH, ZY; funding acquisition: CH, DX; investigation: CH, DX; methodology: CH, DX; project administration: CH, DX; software: CH, HB, DX; supervision: CH, DX; validation: XM, DX, WB; writing: CH, XM, HB. All the authors have read and agreed to the published version of the manuscript.

Financial Support

This study was supported by the National Natural Science Foundation of China (Grant No. 42376011), National Key R&D Plan Program (No.2017YFC0305804).

Competing Interests

The contact author has declared that none of the authors has any competing interests.

Acknowledgements

We acknowledge all the colleagues and project members who have contributed to the design of UGs and AUVs, the sea experiments and data processing in the past. Many scientists, engineers and students have participated in active surveys and mappings.

Disclaimer

Publisher's note: Copernicus Publications remains neutral with regard to jurisdictional claims made in the text, published maps, institutional affiliations, or any other geographical representation in this paper. While Copernicus Publications makes every effort to include appropriate place names, the final responsibility lies with the authors.

References:

Bonnici, J., and Billant, P.: Evolution of a vortex in a strongly stratified shear flow. Part 1. Asymptotic analysis, J. Fluid Mech., 893, https://doi.org/10.1017/jfm.2020.226, 2020.

Caffaz, A., Caiti, A., Casalino, G., and Turetta, A.: The hybrid glider/AUV folaga, IEEE Robot. Autom. Mag., 17(1), 31~44, https://doi.org/10.1109/MRA.2010.935791, 2010.

Chelton, D., Schlax, M., Samelson, R., and de Szoeke, R. Global observations of large oceanic eddies, Geophys. Res. Lett., 34(15), L15606, https://doi.org/10.1029/2007GL030812, 2007.

Chelton, D., Schlax, M., and Samelson, R.: Global observations of nonlinear mesoscale eddies, Prog. Oceanogr., 91(2), 167–216, https://doi.org/10.1016/j.pocean.2011.01.002. 2011.

Chen, G., Hou, Y., and Chu, X.: Mesoscale eddies in the South China Sea: Mean properties, spatiotemporal variability, and impact on thermohaline structure. J. Geophys. Res.-Oceans, 116, C06018, https://doi.org/10.1029/2010JC006716, 2011.

Chu, P., Chen, Y., and Lu, S.: Wind-driven South China Sea deep basin warm-core/cool-core eddies, J. Oceanogr., 54(4), 347-360, https://doi.org/10.1007/bf02742619, 1998.

Chu, P. and Fan, C.: Optimal linear fitting for objective determination of ocean mixed layer depth from glider profiles, J. Atmos. Ocean. Technol., 27, 1893–1898, https://doi.org/10.1175/2010JTECHO804.1, 2010.

Dale, W.: Winds and drift currents in the South China Sea, Malayan Journal of Tropical Geography, 8, 1-31, 1956.

Dong, C., Mcwilliams, J., C., Liu, Y., and Chen D.: Global heat and salt transports by eddy movement, Nat. Commun., 5(2), 3294, https://doi.org/10.1038/ncomms4294, 2014.

Dong, J. and Zhong, Y.: The spatiotemporal features of submesoscale processes in the northeastern South China Sea, Acta Oceanol. Sin., 37(11), 8-18, https://doi.org/10.1007/s13131-018-1277-2, 2018.

Eriksen, C. C., Osse, T. J., Light, R. D., Wen, T., Lehmann, T. W., Sabin, P. L., Ballard, J. W., and Chiodi, A. M.: Seaglider: A long range autonomous underwater vehicle for oceanographic research, IEEE J. Ocean. Eng., 26(4), 424~436, https://doi.org/10.1109/48.972073, 2001.

Fang, W., Fang, G., Shi, P., Huang, Q., and Xie, Q.: Seasonal structures of upper layer circulation in the southern South China Sea from in situ observations, J. Geophys. Res.-Oceans, 107(C11), 23-1-23-2, https://doi.org/10.1029/2002JC001343, 2002.

Fofonoff, N.P. and Millard, R.C.: Algorithms for computation of fundamental properties of seawater, Unesco Tech. Pap. in Mar. Sci., 44, 53, https://doi.org/10.1016/j.saa.2012.12.093, 1983.

Fox-Kemper, B., Ferrari, R., and Hallberg, R.: Parameterization of mixed layer eddies. Part I: Theory and diagnosis, J. Phys. Oceanogr., 38(6), 1145-1165, https://doi.org/10.1175/2007JPO3792.1, 2008.

Gao, Z., Chen, Z., Huang, X., Yang, H., Wang, Y., Ma, W., and Luo, C.: Estimating the energy flux of internal tides in the northern South China Sea using underwater gliders, J. Geophys. Res.-Oceans, 129, e2023JC020385, https://doi.org/10.1029/ 2023JC020385, 2024.

Gaube, P., Chelton, D. B., Samelson, R. M., Schlax, M. G., and O'Neill, L. W.: Satellite Observations of Mesoscale Eddy-Induced Ekman Pumping, J. Phys. Oceanogr., 45, 104–132, https://doi.org/10.1175/JPO-D-14-0032.1, 2015.

He, Q., Zhan, H., Cai, S., He, Y., Huang, G., and Zhan, W.: A new assessment of mesoscale eddies in the South China Sea: surface features, three-dimensional structures, and thermohaline transports, J. Geophys. Res.-Oceans, 123(7), 4906-4929,

https://doi.org/10.1029/2018JC014054, 2018.
He, Q., Zhan, H., Xu, J., Cai, S., Zhan, W., Zhou, L., and Zha, G.: Eddy-induced chlorophyll anomalies in the western South China Sea, J. Geophys. Res.-Oceans, 124, https://doi.org/10.1029/2019JC015371, 2019.
He, Y., Xie, J., and Cai, S.: Interannual variability of winter eddy patterns in the eastern South China Sea, Geophys. Res. Lett., 43(10), 5185-5193, https://doi.org/10.1002/2016GL068842, 2016.
Hobson, B. W., Bellingham, J. G., Kieft, B., McEwen, R., Godin, M. and Zhang, Y.: Tethys-class long range AUVs - extending the endurance of propeller-driven cruising AUVs from days to weeks, in: IEEE/OES Autonomous Underwater Vehicles (AUV), Southampton, UK, 24-27 Sept. 2012, 1-8, https://doi.org/10.1109/AUV.2012.6380735, 2012.
Hu, Z., Lin, H., Liu Z., Cao Z., Zhang F., Jiang Z., Zhang Y., Zhou K., and Dai M.: Observations of a filamentous intrusion and vigorous submesoscale turbulence within a cyclonic mesoscale eddy, J. Phys. Oceanogr., 53(6), 1615–1627, https://doi.org/10.1175/JPO-D-22-0189.1, 2023.
Huang, Y., Qiao, J., Yu, J., Wang, Z., Xie, Z., and Liu, K.: Sea-Whale 2000: a long-range hybrid autonomous underwater vehicle for ocean observations, in: OCEANS 2019 - Marseille, Marseille, France, 17-20 June 2019, 1-6, https://doi.org/10.1109/OCEANSE.2019.8867050, 2019.
Hwang, C. and Chen, S.: Circulations and eddies over the South China Sea derived from TOPEX/Poseidon altimetry, J. Geophys. Res.-Oceans, 105(C10), 23943-23965, https://doi.org/10.1029/2000JC900092, 2000.
Li, H., Xu, F., and Wang, G.: Global mapping of mesoscale eddy vertical tilt, J. Geophys. Res.-Oceans, 127, e2022JC019131, https://doi.org/10.1029/2022JC019131, 2022.
Li, L., Worth. D., Nowlin, J., and Su. J.: Anticyclonic rings from the Kuroshio in the South China Sea, Deep-Sea Res. Part I-Oceanogr. Res. Pap., 45, 1469-1482, https://doi.org/10.1016/s0967-0637(98)00026-0, 1998.
Lin, X., Dong, C., Chen, D., Liu, Y., Yang, J., Zou, B., and Guan, Y.: Three-dimensional properties of mesoscale eddies in the South China Sea based on eddy-resolving model output, Deep-Sea Res. Part I-Oceanogr. Res. Pap., 99, 46-64, https://doi.org/10.1016/j.dsr.2015.01.007, 2015.
Lin, P., Wang, F., Chen, Y., and Tang, X.: Temporal and spatial variation characteristics of eddies in the South China Sea I: Statistical analyses, Acta Oceanol. Sin., 29(3), 14-22, https://doi.org/10.3321/j.issn:0253-4193.2007.03.002, 2007.
McWilliams, J.: Submesoscale currents in the ocean, Proc. R. Soc. A-Math. Phys. Eng. Sci., 472, 20160117, http://dx.doi.org/10.1098/rspa.2016.0117, 2016.
Morison, J., Andersen, R., Larson, N., D'Asaro, E., and Boyd, T.: The correction for thermal-lag effects in Sea-Bird CTD data, J. Atmos. Ocean. Technol., 11, 1151–1164, https://doi.org/10.1175/1520-0426(1994)011,1151:TCFTLE.2.0.CO;2, 1994.
Morrow, R., Birol, F., Griffin, D., and Sudre, J.: Divergent pathways of cyclonic and anti-cyclonic ocean eddies, Geophys. Res. Lett., 31(24), L24311, https://doi.org/10.1029/2004gl020974, 2004.
Nan, F., He, Z., Zhou, H., and Wang, D.: Three long-lived anticyclonic eddies in the northern South China Sea, J. Geophys. Res.-Oceans, 116(5), C05002, https://doi.org/10.1029/2010JC006790, 2011.
Ni, Q., Zhai, X., Wilson, C., Chen, C., and Chen, D.: Submesoscale eddies in the South China Sea, Geophys. Res. Lett., 48, e2020GL091555, https://doi.org/10.1029/2020GL091555, 2021.

Oey, L.: Eddy- and wind-forced shelf circulation, J. Geophys. Res., 100(C5), 8621–8637, https://doi.org/10.1029/95JC00785, 1995.

Okkonen, S., Weingartener, T., Danielson, S., Musgrave, D., and Schmidt, G. M.: Satellite and hydrographic observations of eddy-induced shelf-slope exchange in the northwestern Gulf of Alaska, J. Geophys. Res., 108(C2), 3033, https://doi.org/10.1029/2002JC001342, 2003.

Osse, T. J. and Eriksen, C. C.: The deepglider: a full ocean depth glider for oceanographic research, in: OCEANS 2007, Aberdeen, UK, 18-21 June 2007, 1~12, https://doi.org/10.1109/OCEANS.2007.4449125, 2007.

Qi, Y., Shang, C., Mao, H., Qiu, C., and Shang, X.: Spatial structure of turbulent mixing of an anticyclonic mesoscale eddy in the northern South China Sea, Acta Oceanol. Sin., 39(11), 69-81, https://doi.org/10.1007/s13131-020-1676-z, 2020.

Qiao, J., Qiu, C., Wang, D., Huang, Y., Zhang, X., and Huang, Y.: Multi-stage Development within Anisotropy Insight of an Anticyclone Eddy Northwestern South China Sea in 2021, Geophys. Res. Lett., 50, 19, https://doi.org/10.1029/2023GL104736, 2023.

Qiu, C., Mao, H., Yu, J., Xie, Q., Wu, J., Lian, S., and Liu, Q.: Sea surface cooling in the Northern South China Sea observed using Chinese Sea-wing Underwater Glider Measurements, Deep-Sea Res. Part I-Oceanogr. Res. Pap., 105, 111-118, https://doi.org/10.1016/j.dsr.2015.08.009, 2015.

Qiu, C., Mao, H., Liu, H., Xie, Q., Yu, J., Su, D., Ouyang, J., and Lian, S.: Deformation of a warm eddy in the northern South China Sea, J. Geophys. Res.-Oceans, 124, 5551-5564, https://doi.org/10.1029/2019JC015288, 2019a.

Qiu, C., Mao, H., Wang, Y., Su, D., and Lian, S.: An irregularly shaped warm eddy observed by Chinese underwater gliders, J. Oceanogr., 75, 139-148, https://doi.org/10.1007/s10872-018-0490-0, 2019b.

Qiu, C., Liang, H., Huang, Y., Mao, H., Yu, J., Wang, D., and Su, D.: Development of double cyclonic mesoscale eddies at around Xisha Islands observed by a ‘Sea-Whale 2000’ autonomous underwater vehicle, Appl. Ocean Res., 101, 102270, https://doi.org/10.1016/j.apor.2020.102270, 2020.

Qiu, C., Yi, Z., Su, D., Wu, Z., Liu, H., Lin, P., He, Y., and Wang, D.: Cross-slope heat and salt transport induced by slope intrusion eddy’s horizontal asymmetry in the northern South China Sea, J. Geophys. Res.-Oceans, 127(9), https://doi.org/10.1029/2022JC018406, 2022.

Qiu, C., Yang, Z., Feng, M., Yang, J., Rippeth, T. P., Shang, X., Sun, Z., Jing, C., and Wang, D.: Observational energy transfers of a spiral cold filament within an anticyclonic eddy, Prog. Oceanogr., 220, 1.1-1.12, https://doi.org/10.1016/j.pocean.2023.103187, 2024a.

Qiu, C., Du, Z., Tang, H., Yi, Z., Qiao, J., Wang, D., Zhai, X., and Wang, W.: A High-Resolution Temperature-Salinity Dataset Observed by Autonomous Underwater Vehicles for the Evolution of Mesoscale Eddies and Associated Submesoscale Processes in South China Sea [data set], https://doi.org/10.57760/sciencedb.11996, 2024b.

Rainville, L., Lee, C., Arulananthan, K., Jinadasa, S., Fernando, H., Priyadarshani, W., and Wijesekera, H.: Water mass exchanges between the Bay of Bengal and Arabian Sea from multiyear sampling with autonomous gliders, J. Phys. Oceanogr., 52, 2377–2396, https://doi.org/10.1175/JPO-D-21-0279.1, 2022.

Rudnick, D. L., Davis, R. E., Eriksen, C. C., Fratantoni, D. M., Perry, M. J.: Underwater Gliders for Ocean Research, Mar. Technol. Soc. J., 38(2), 73-84, https://doi.org/10.4031/002533204787522703, 2004.

Shang, X., Shu, Y., Wang, D., Yu, J., Mao, H., Liu, D., Qiu, C., and Tang, H.: Submesoscale motions driven by down-front wind around an anticyclonic eddy with a cold core, J. Geophys. Res.-Oceans, 128, e2022JC019173, https://doi.org/10.1029/2022JC019173, 2023.

Sherman, J., Davis, R. E., Owens, W. B. and Valdes, J.: The autonomous underwater glider "Spray", IEEE J. Ocean Eng., 26(4), https://doi.org/10.1109/48.972076 437~446, 2001.

Shu, Y., Xiu, P., Xue, H., Yao, J., and Yu, J.: Glider-observed anticyclonic eddy in northern South China Sea, Aquat. Ecosyst. Health Manag., 19(3), 233–241, https://doi.org/10.1080/14634988.2016.1208028, 2016.

Su, D., Lin, P., Mao, H., Wu, J., Liu, H., Cui, Y., and Qiu, C.: Features of slope intrusion mesoscale eddies in the northern South China Sea, J. Geophys. Res.-Oceans, 125, e2019JC015349, https://doi.org/ 10.1029/2019JC015349, 2020.

Tang, H., Shu, Y., Wang, D., Xie, Q., Zhang, Z., Li, J., Shang, X., Zhang, O., and Liu, D,: Submesoscale processes observed by high-frequency float in the western South China Sea, Deep-Sea Res. Part I-Oceanogr. Res. Pap., 103896, https://doi.org/10.1016/j.dsr.2022.103896, 2022.

Thomas, L., Taylor, J., Ferrari, R., and Terrence M.: Symmetric instability in the Gulf Stream. Deep-Sea Res. Part II-Top. Stud. Oceanogr., 91, 96-110, https://doi.org/10.1016/j.dsr2.2013.02.025, 2013.

Todd, R.E. and Ren, A.S.: Warming and lateral shift of the Gulf Stream from in situ observations since 2001, Nat. Clim. Chang., 13, 1348–1352, https://doi.org/10.1038/s41558-023-01835-w, 2023.

Wang, G., Su, J., and Chu, P.: Mesoscale eddies in the South China Sea observed with altimetry, Geophys. Res. Lett., 30(21), 2121, https://doi.org/10.1029/2003GL018532, 2003.

Wang, G., Chen, D., and Su, J.: Winter eddy genesis in the eastern South China Sea due to orographic wind jets, J. Phys. Oceanogr., 38(3), 726–732, https://doi.org/10.1175/2007jpo3868.1, 2008.

Wang, Q., Zeng, L., Li, J., Chen, J., He, Y., Yao, J., Wang, D., and Zhou, W.: Observed Cross-Shelf Flow Induced by Mesoscale Eddies in the Northern South China Sea, J. Phys. Oceanogr., 48, 1609–1628, https://doi.org/10.1175/JPO-D-17-0180.1, 2018.

Wang, D., Xu, H., Lin, J., and Hu, J.: Anticyclonic eddies in the northeastern South China Sea during winter of 2003/2004, J. Oceanogr., 64(6), 925-935, https://doi.org/10.1007/s10872-008-0076-3, 2008.

Wang, J.: The warm-core eddy in the northern South China Sea, I. Preliminary observations on the warm-core eddy, Acta Oceanogr. Taiwanica, 18, 1987.

Wu, J., Zhang, M., and Sun, X.: Hydrodynamic characteristics of the main parts of a hybrid-driven underwater glider PETREL, in: Autonomous Underwater Vehicles, edited by: Nuno A. Cruz, The Institution of Engineering and Technology, London, UK, https://doi.org/10.5772/24750, 2011.

Xiu, P., Chai, F., Shi, L., Xue, H., and Chao, Y.: A census of eddy activities in the South China Sea during 1993-2007, J. Geophys. Res.-Oceans, 115, C03012, https://doi.org/10.1029/2009JC005657, 2010.

Xu, J. and Su, J.: Hydrographic analysis of Kuroshio intrusion into the South China Sea II: Observations during August to September 1994, Tropical Oceanography, 2, 1-23, 1997 (in

Chinese).
Yang, H. and Liu, Q.: The seasonal features of temperature distributions in the upper layer of the South China Sea, Oceanologia et Limnologia Sinica, 29(5), 501-507, 1998 (in Chinese).
Yang, Q., Nikurashin, M., Sasaki, H., Sun, H., and Tian, J.: Dissipation of mesoscale eddies and its contribution to mixing in the northern South China Sea, Sci. Rep., 9, https://doi.org/10.1038/s41598-018-36610-x, 2019.
Yi, Z., Wang, D., Qiu, C., Mao, H., Yu, J., and Lian, S.: Variations in dissolved oxygen induced by a tropical storm within an anticyclone in the Northern South China Sea. J. OCEAN UNIV., 21(5), 1084-1098, https://doi.org/10.1007/s11802-022-4992-4, 2022.
Yi, Z., Qiu, C., Wang, D., Cai, Z., Yu, J., and Shi, J.: Submesoscale kinetic energy induced by vertical buoyancy fluxes during the tropical cyclone Haitang. J. Geophys. Res.-Oceans, 129, e2023JC020494, https://doi.org/10.1029/2023JC020494, 2024.
Yu, J., Zhang, A, Jing, W. Chen, Q. Tian, Y., and Liu, W.: Development and Experiments of the Sea-Wing Underwater Glider, China Ocean Eng., 25(4), 721-736, https://doi.org/10.1007/s13344-011-0058-x, 2011.
Zhang, Z. and Qiu, B.: Evolution of submesoscale ageostrophic motions through the life cycle of oceanic mesoscale eddies, Geophys. Res. Lett., 45(21), 11847-11855, https://doi.org/10.1029/2018GL080399, 2018.
Zhang, Z., Tian, J., Qiu, B., Zhao, W., Chang, P., and Wu, D.: Observed 3D Structure, Generation, and Dissipation of Oceanic Mesoscale Eddies in the South China Sea, Sci. Rep., 6(1), 24349, https://doi.org/10.1038/srep24349, 2016.
Zhang, Z., Zhao, W., Qiu, B., and Tian, J.: Anticyclonic eddy sheddings from Kuroshio loop and the accompanying cyclonic eddy in the Northeastern South China Sea, J. Phys. Oceanogr., 47(6), 1243-1259, https://doi.org/10.1175/JPO-D-16-0185.1, 2017.